Chapter 2
CFD Method for Modelling Gurney Flaps

Vasileios Pastrikakis, Mark Woodgate, and George Barakos

2.1 Numerical Methods

The present work presents the necessary extensions to the HMB2 CFD solver of Liverpool to allow modelling of Gurney flaps either fixed or actuated. Several methods of implementing Gurney flaps were investigated, and it was found that modelling the flap as a discontinuity in the mesh produced results close to what Gurney flaps of some thickness would give. This also allowed a simple implementation of actuated Gurneys, and the method is demonstrated here for 2D sections, finite span wings and rotors in hover and forward flight.

If a Gurney flap is to be added to a rotor blade, a passive device will lead to a fully deployed Gurney through the whole azimuth as in the study of Min et al. (2009), while an active Gurney could be deployed on demand. In that case, it could be fully deployed in hover flight to increase the lift capability of the rotor, while in forward flight, it could be retracted at the advancing side and deployed actively at the retreating side of the rotor. Also, due to the practicalities of implementing Gurney flaps on rotors, several configurations are possible, and the method presented can cope with these various flap designs. Two possible Gurney flap configurations are shown in Fig. 2.1.

In the first configuration, the Gurney flap is allowed to move vertically above and below the aerofoil. One obvious drawback of this option, if the Gurney is not telescopic, is that to obtain even 2–3 % c Gurney flaps, these should be placed around the 90 % chord of the aerofoil. This would reduce the overall effectiveness of

V. Pastrikakis
Consulting Engineer, SoftInWay Switzerland GmbH
e-mail: v.pastrikakis@gmail.com

M. Woodgate • G. Barakos (✉)
University of Glasgow, Glasgow, UK
e-mail: mark.woodgate@glasgow.ac.uk; George.Barakos@glasgow.ac.uk

Fig. 2.1 Proposed Gurney flap configurations

Configuration A
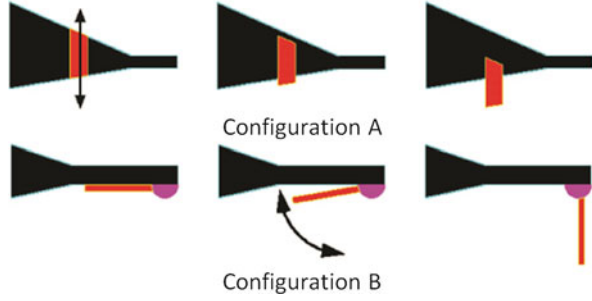
Configuration B

a fixed sized Gurney as discussed in the study of Wang et al. (2008). Configuration (*b*) is hinged at the trailing edge of the lower surface, and the Gurney is closed by rotating clockwise towards the leading edge.

2.1.1 HMB Solver

The HMB2 CFD solver (Steijl and Barakos 2008a, b; Steijl et al. 2006) was employed for this work. HMB2 solves the Navier-Stokes equations in integral form using the arbitrary Lagrangian-Eulerian formulation for time-dependent domains with moving boundaries:

$$\frac{d}{dt}\int_{V(t)} \boldsymbol{w}\, dV + \int_{\partial V(t)} (\boldsymbol{F_i}(\boldsymbol{w}) - \boldsymbol{F_v}(\boldsymbol{w}))\, \boldsymbol{n}\, dS = \boldsymbol{S} \qquad (2.1)$$

The above equations form a system of conservation laws for any time-dependent control volume $V(t)$ with boundary $\partial V(t)$ and outward unit normal $\boldsymbol{n}$. The vector of conserved variables is denoted by $\boldsymbol{w} = [\rho,\ \rho u,\ \rho v,\ \rho w,\ \rho E]^T$, where ρ is the density, u, v, w are the Cartesian velocity components and E is the total internal energy per unit mass. $\boldsymbol{F_i}$ and $\boldsymbol{F_v}$ are the inviscid and viscous fluxes, respectively. For hovering rotors, the grid is fixed, and a source term, $\boldsymbol{S} = [0, -\rho\boldsymbol{\omega} \times \boldsymbol{u}_h,\ 0]^T$, is added to compensate for the inertial effects of the rotation. $\boldsymbol{u}_h$ is the local velocity field in the rotor-fixed frame of reference.

The non-inertial frame of reference used here has two benefits over a rotating frame of reference: firstly, the energy equation is unchanged by the rotation vector $\boldsymbol{\omega}$ and, secondly, a vanishing 'undisturbed' velocity field occurs in contrast to the position-dependent 'undisturbed' velocity field in the rotating frame of reference, which is given by $-\boldsymbol{\omega} \times \boldsymbol{r}$.

Equation (2.1) is discretised using a cell-centred finite volume approach on structured multiblock grids. The spatial discretisation leads to a set of equations in time:

$$\frac{\partial}{\partial t}\left(\boldsymbol{w}_{i,j,k} V_{i,j,k}\right) = -\boldsymbol{R}_{i,j,k}\left(\boldsymbol{w}_{i,j,k}\right) \tag{2.2}$$

where $\boldsymbol{w}$ and $\boldsymbol{R}$ are the vectors of cell variables and residuals, respectively. Here, i, j, k are the cell indices in each of the grid blocks, and $V_{i,j,k}$ is the cell volume. The convective terms are discretised using Osher's upwind scheme (Osher and Chakravarthy 1983), MUSCL variable interpolation is used to provide high-order accuracy, and the van Albada limiter (Albada et al. 1982) is employed to prevent spurious oscillations near steep gradients. Boundary conditions are set using ghost cells on the exterior of the computational domain. For viscous flow simulations, ghost values are extrapolated at solid boundaries ensuring that the velocity takes on the solid wall velocity. Implicit time integration is employed, and the resulting linear system of equations is solved using a preconditioned generalised conjugate gradient method. For unsteady simulations, an implicit dual-time stepping method is used, based on the pseudo-time integration approach by Jameson (1991). The HMB2 method has been validated for a range of rotorcraft applications and has demonstrated good accuracy and efficiency for very demanding flows. Examples of work with HMB2 can be found in references (Steijl and Barakos 2008a, b). Several rotor trimming methods are available in HMB2 along with a blade-actuation algorithm that allows for the near-blade grid quality to be maintained on deforming meshes (Steijl et al. 2006).

The HMB2 solver has a library of turbulence closures including several one- and two-equation turbulence models and even non-Boussinesq versions of the k–ω model that is used for this work. Turbulence simulation is also possible using either the large-eddy or the detached-eddy approach. The solver was designed with parallel execution in mind, and the MPI library along with a load-balancing algorithm is used to this end. For multiblock grid generation, the ICEM-CFD Hexa commercial meshing tool is used, and CFD rotor grids with 10–30 million points and thousands of blocks are commonly used.

2.1.2 Modelling Gurney Flaps

2.1.2.1 Proposed Methods

The proposed methods for dealing with the Gurney flaps of Figs. 2.1 and 2.2 are outlined below. It should be noted that the first two methods can be implemented using part of the functionality required in overset grid methods, namely, the ability to apply wall boundary conditions to any cell face when the overset grids intersect each other and the ability to cut a hole into a grid where there is an intersection with a solid. This is shown in the second method in Fig. 2.2b.

The first method (Fig. 2.2a) uses the current grid lines within the block. In the past, when using HMB2, fixed Gurneys have been approximated by setting a solid wall boundary flag between blocks, giving the effect of a very thin flap. The code had to be extended for the active Gurney case. As an example, consider configuration
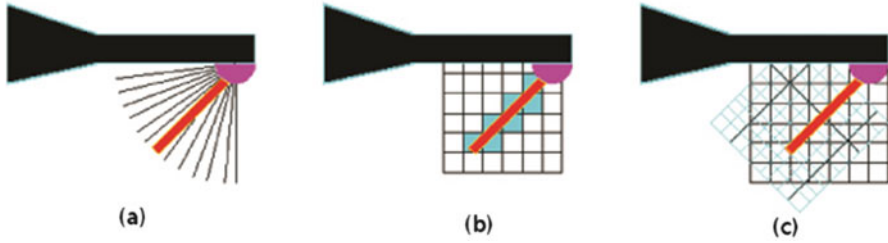
Fig. 2.2 The three possible methods for the solution of the active Gurney flap shown for configuration B of Fig. 2.1. (**a**) Grid lines within the block have been used, (**b**) computational cells are flagged as solid, (**c**) intersecting grids

shown in Fig. 2.2a for a case where a Gurney is aligned with a block boundary. As the Gurney moves, it will violate the requirement of HMB2 CFD solver to have a single boundary condition on each block face. In Fig. 2.2a, as the Gurney rotates, it will need to swap over from one grid line to the next. All configurations of Fig. 2.2 would be possible if the CFD method allows any face within a block to be flagged as a solid wall.

The second method (Fig. 2.2b) is one step closer to the overset grid method. Here cells are flagged as solid if they contain part of the flap. In addition to the functionality of the first method (the ability to flag any cell face as a solid wall), the second method also requires a way of flagging cells, in this case shown in shade (Fig. 2.2b), as non-computational cells or holes. After these holes have been flagged, it is a matter of finding any face that is connected to both a computational cell and a hole and flag that as a solid wall.

The final method (Fig. 2.2c) is to use two overset grids: one associated with the aerofoil and the second associated with the active Gurney. This requires all the functionality of the first two methods with additional information needed within HMB2. Firstly, it is necessary to know which cells in each grid are going to be used for computing the solution. For example, if the choice is the background grid with the minimum number of holes, one needs to know how far does the under-resolved flow next to the Gurney affects the rest of the background solution. HMB2 then requires two extra pieces of information, firstly, which cells are used in the computational domain and, secondly, how is information exchanged between grids.

The problem with moving Gurney flaps is that the solid surface of the Gurney which is surrounded by a fine CFD mesh to resolve the flow will have to come very close to the mesh around the aerofoil. The high aspect ratio and very fine grids required to resolve boundary layer flows made the use of some of the proposed methods difficult.

2.1.2.2 Implementation of the Gurney flaps

This section discusses the different methods of modelling a Gurney flap, each with its own advantages and disadvantages.
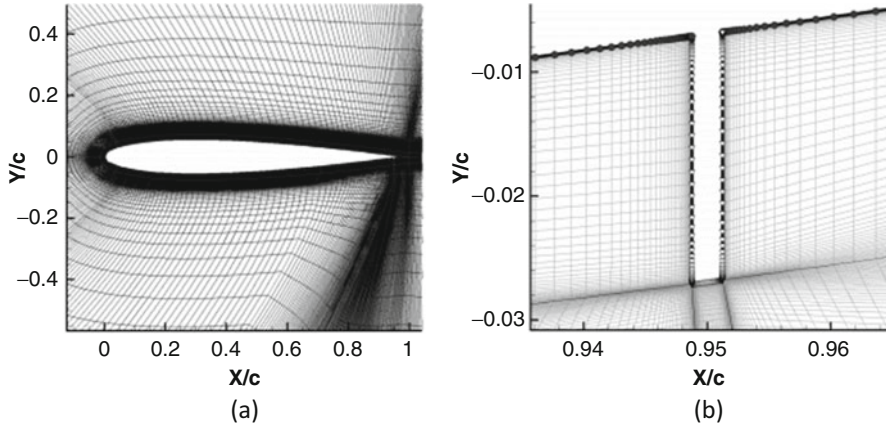
Fig. 2.3 (**a**) Example of a possible blocking for a Gurney at 95 % of the chord. (**b**) Shows a close-up of the Gurney flap. NACA 0012 aerofoil, Gurney size = 2 % chord, Gurney thickness = 0.25 % chord

Gurney Flap Modelled Within the Multiblock Mesh

The most natural way to solve a fixed steady-state Gurney flap is to include the Gurney within the multiblock grid as shown in Fig. 2.3. In this case, the Gurney flap has a well-resolved wall spacing on all sides and hence will be a benchmark solution for comparing it with solutions where the Gurney flap is approximated.

To obtain the loads on the Gurney flap alone and to be able to find its moment about a different point, for example, the Gurney hinge, two additional pieces of information are required. Firstly, a special boundary condition tag is used so the Gurney flap is identified. Secondly, additional Gurney-specific input is necessary to inform the CFD solver that computations are to be performed with a Gurney flap of a specific actuation. Figure 2.3b shows the two boundaries that need to be integrated separately for the calculation of the loads. The boundary for the aerofoil is highlighted with the solid line with the black dots, while the Gurney flap boundary is shown as the solid line with the white gradient symbol.

Gurney Flap Modelled Using Viscous Wall Boundary Condition Across a Block Face

In this case, the Gurney is assumed to be thin and is modelled along a block boundary. Since it is a restriction within HMB2 that each block face can only have one type of condition applied to it, the whole face must be part of the Gurney flap. The case, however, is computed in exactly the same way as if the Gurney had some thickness as explained in Sect. 2.1.2.2.1. The advantage of this method is that no additional effort is needed in terms of mesh generation. On the other hand, the
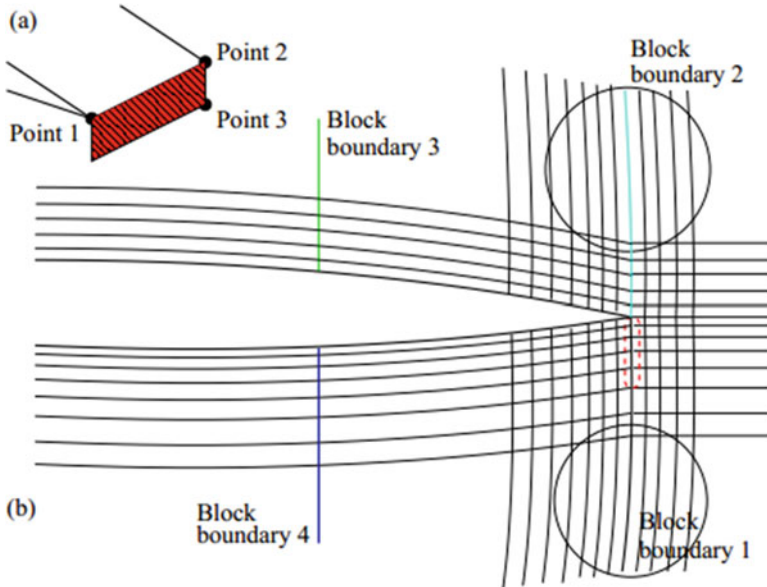
Fig. 2.4 Method for flagging a Gurney flap: (**a**) Gurney plane definition and (**b**) elimination of block boundaries 3 and 4 for not meeting the distance requirements and part of boundaries 1 and 2 for not meeting the angle requirements. Only the cell faces of the accepted block boundaries that are inside the Gurney plane will be flagged as solid (Gurney flap)

Gurney is assumed to have no thickness, and its size must coincide with the size of a block face. Figures 2.4 and 2.5 present the concept along with its extension to several cases discussed below.

Gurney Flap Modelled Using Blocked Cells Next to a Block Face

To overcome the restrictions of the previous method regarding the size of the Gurney flap, a new way of modelling thin Gurneys has been added to HMB2. This allows for any number of cells on a block face to be flagged as blocked. This means that the same grid can be used for different size flaps as well as allowing unsteady deployment of Gurney flaps along block interfaces. Figures 2.4 and 2.5 present the idea using schematics of cells and block interfaces.

For an actuated Gurney, it is important to have a robust method for blocking the correct cells. This process can be framed as a collection of computational geometry problems which have to work robustly in the very thin, high aspect ratio, cells that make up the first part of any boundary layer mesh. The algorithm is a four-stage process.

Part one is to define a planar Gurney with three points; the remaining stages are then computational geometry problems which eliminate cells until just those
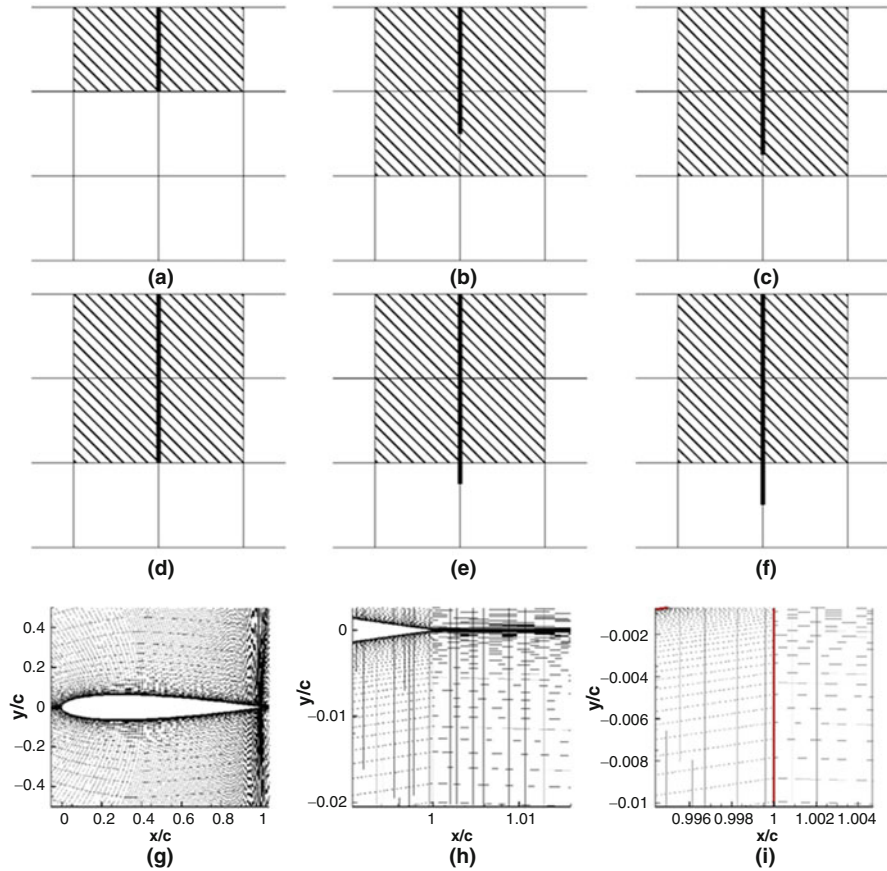
Fig. 2.5 Flagging of the cells (*shaded*) that require a wall boundary condition applied to their face to model Gurney flap (shown in *solid black line*). The Gurney flap can change in length without a change in the cells flagged as blocked. Minimal changes are needed in the CFD mesh (**g**, **h**), and the Gurney flap can be seen in (**i**)

representing the Gurney remain. Figure 2.4 explains how the cell faces are finally flagged as a Gurney flap. First, the block boundaries 3 and 4 are excluded as they do not meet the distance requirements between the centroid of each cell face and the planar Gurney, set by the user. Then, parts of the boundaries 1 and 2 which are inside a circle are also excluded as the angle between the normal to the face and the normal to the Gurney does not meet another user-specified tolerance. Finally, the remaining cell centres of the faces are projected onto the Gurney plane, and if they are inside the polygon formed by the Gurney, they are flagged as blocked. These cells are surrounded by the dashed line at the trailing edge of the aerofoil shown in Fig. 2.4b.

Resolution of the Length of the Gurney

For a Gurney flap of fixed height, it is always possible to place a grid point at the end of the Gurney, and hence no approximation is made if the method of blocked cell faces is used. However, if the Gurney does not end at a grid point, the semi-blocked cells must be treated in a special way. The first method is as follows: if the projection of the centre of a cell faces onto the plane described by the Gurney flap is within the Gurney, then it is flagged as blocked else it is flagged as open. Examples of this method were shown in Fig. 2.5a–f. The Gurney, shown in bold solid line, is assumed to be infinity thin and close to a block boundary, the shaded cells are flagged, and a viscous wall boundary condition is applied to the face that coincides with the Gurney. Figure 2.5a–f shows that as the Gurney extends in length, more of the cells are flagged as blocked. The length of the Gurney can only be resolved to the size of the mesh cell at its end.

To demonstrate this behaviour, three cases were computed using a Gurney at the trailing edge of a NACA 0012 aerofoil of a length approximately 1 % of the aerofoil chord. Figure 2.5g–i shows the grid and the region around the end of the Gurney flap. It can be seen that this grid has a large number of points normal to the Gurney surface to help resolve the flow.

The discretisation effect of an actuated Gurney flap was addressed with a technique that allows the flux between cells to be split according to the area of a cell exposed to the flow. The idea is to compute first the fraction of the area covered by the Gurney flap over the area of the cell face. The flux f_1 is computed on the interface between the two cells assuming no wall, and then, the flux f_2 is computed as if there is a wall boundary at the face of the cell. Finally, these fluxes are weighted by the fraction of the areas as described in the following equation:

$$f = f_1 \left(1 - \Delta A\right) + f_2 \Delta A \qquad (2.3)$$

An example of the part-flux method is shown in Fig. 2.6. In Fig. 2.6a, a simple schematic of two cells is presented where a Gurney flap covers the shaded area. Figure 2.6b presents how these cells are treated in the code during the two different calculations of the fluxes before weighting them.

Figures 2.7 and 2.8 present the comparison of the results obtained for a NACA 0012 with a 2 % chord actuated Gurney flap between the full-flux and the part-flux method. Judging from Fig. 2.7, the variation of the change of the lift coefficient of the aerofoil is smoother when it is computed with the part-flux method (solid line), while with the full-flux method, rapid changes of the lift are observed while changing the size of the Gurney flap (dotted line). In Fig. 2.8, the U and V components of the velocity are presented near the Gurney flap with contours for the full-flux method and lines for the part-flux method.
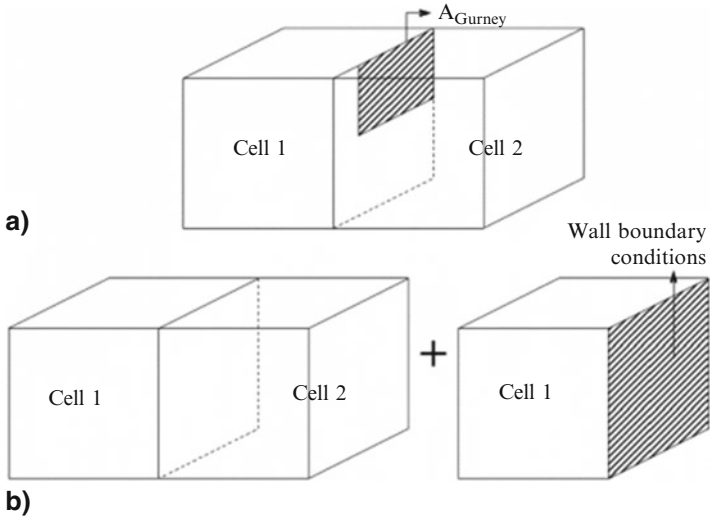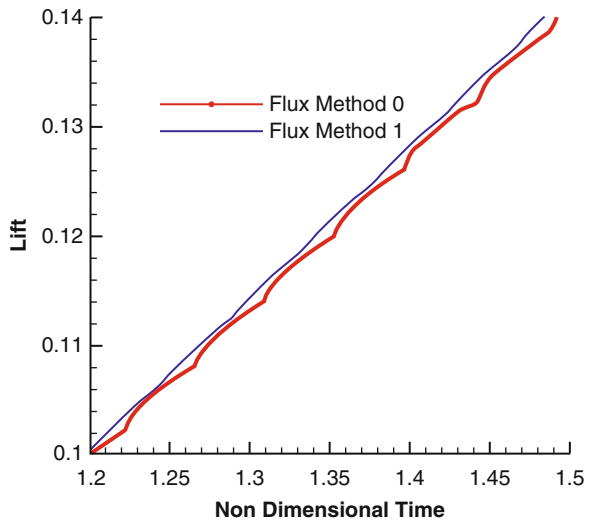
Fig. 2.6 Part-flux method description: (**a**) schematic of a Gurney flap covered part of the face between two cells and (**b**) calculation of the fluxes twice before weighting them

Fig. 2.7 Lift coefficient between the part-flux (method 1) and the full-flux (method 0) methods for a NACA 0012 aerofoil with an actuated 2 % chord Gurney flap. $M = 0.2$, Re $= 2.1 \times 10^6$, $\alpha = 0$ deg, $k - \omega$ SST (Menter 1994)

Swinging Gurney

For such a case, a blocking topology is seen in Fig. 2.9. The figure shows the mesh around a NACA 0012 aerofoil with a swinging Gurney located at 95 % of the chord and the modification of the blocks near the trailing edge of the aerofoil.

The method used to flag cell faces as blocked for a swinging Gurney is presented in Fig. 2.10. First, the code calculates the radius of the Gurney in the same way it
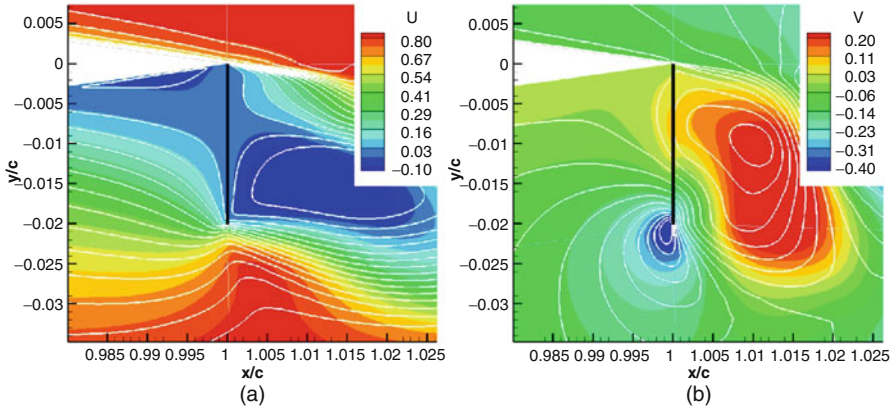
Fig. 2.8 Viscous flow around a NACA 0012 aerofoil with an actuated 2 % chord Gurney flap. The colour contours represent the solution with the full-flux method, and the white contours represent the solution with part-fluxes. $M = 0.2$, Re $= 2.1 \times 10^6$, $\alpha = 0$ deg, $k - \omega$ SST (Menter 1994). (**a**) Contours of U-velocity component. (**b**) Contours of V-velocity component

Fig. 2.9 Example of a possible blocking for a swinging Gurney at 95 % of the chord and a near view of the topology
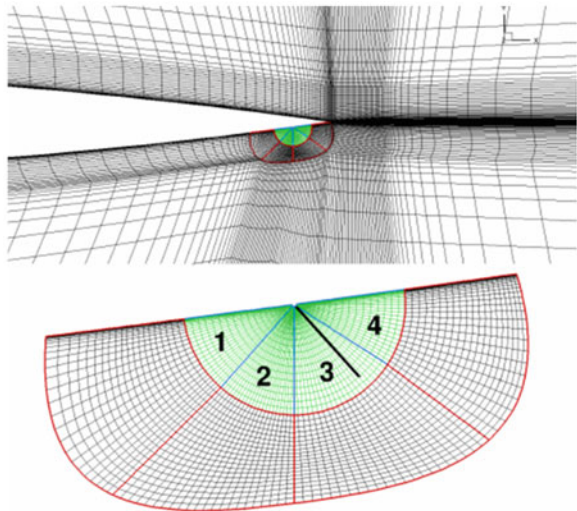
calculated the height of the Gurney during the linear actuation. At every time step, it then computes the angle of the Gurney, and it defines the new Gurney plane as shown in Fig. 2.10a. Then for the blocks 1–4 in the near view of Fig. 2.9, the code flags the cells behind and in front of the Gurney with −1 and 1, respectively, if they are inside the radius of the Gurney or with −2 and 2 if they are outside as presented in Fig. 2.10b. Next, the code sweeps along the grid lines and averages the flags on the nodes. The nodes with zero value will form the Gurney flap, and if the sum of
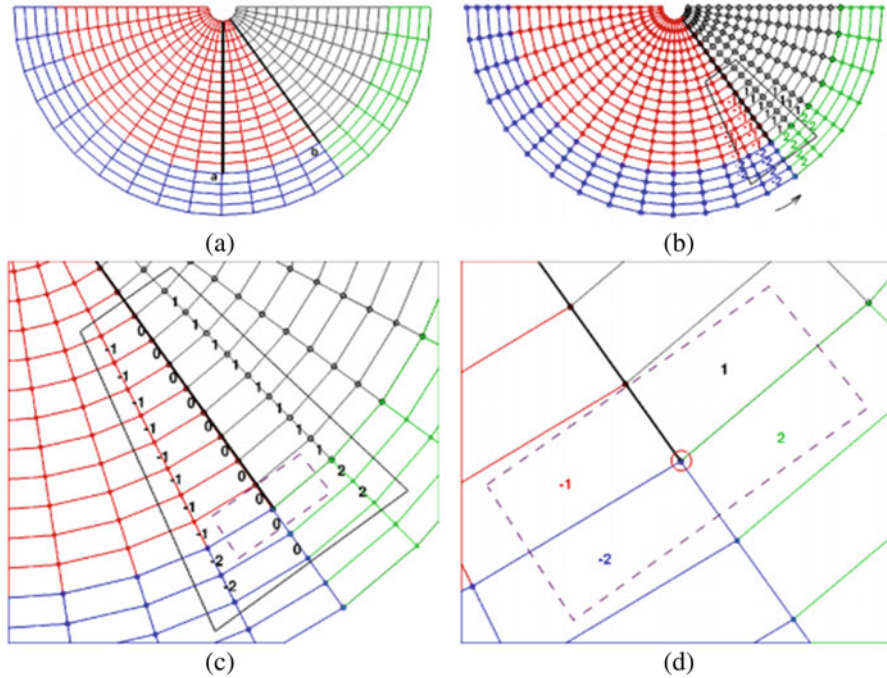
Fig. 2.10 Description of method for flagging wall faces for a swinging Gurney case with HMB2. (**a**) Definition of the Gurney plane. (**b**) Flagging cells behind and in front of the Gurney. (**c**) Average the flags on the nodes. (**d**) Definition of the end point of the Gurney

the absolute values of the four neighbour cells of a node is 6, then this node is the end of the Gurney flap as presented in Fig. 2.10c, d. Then all the cell faces up to the end point are flagged as blocked.

2.1.3   Results for Gurney Flaps in Two Dimensions

The following section demonstrates the different methods for modelling Gurney flaps that were outlined in Sect. 2.1.2.

2.1.3.1   Fixed Gurney Flap

The grid used for these calculations can be seen in Fig. 2.11. The aerofoil used is a NACA 0012 at $M = 0.2$, $\mathrm{Re} = 2.1 \times 10^6$, $\alpha = 0$ deg. Different Gurney sizes were used from 0.5 % c up to 2 % c, and the span of the Gurney was 1 chord. The aerofoil trailing edge was refined more than the normal to resolve the boundary layer of
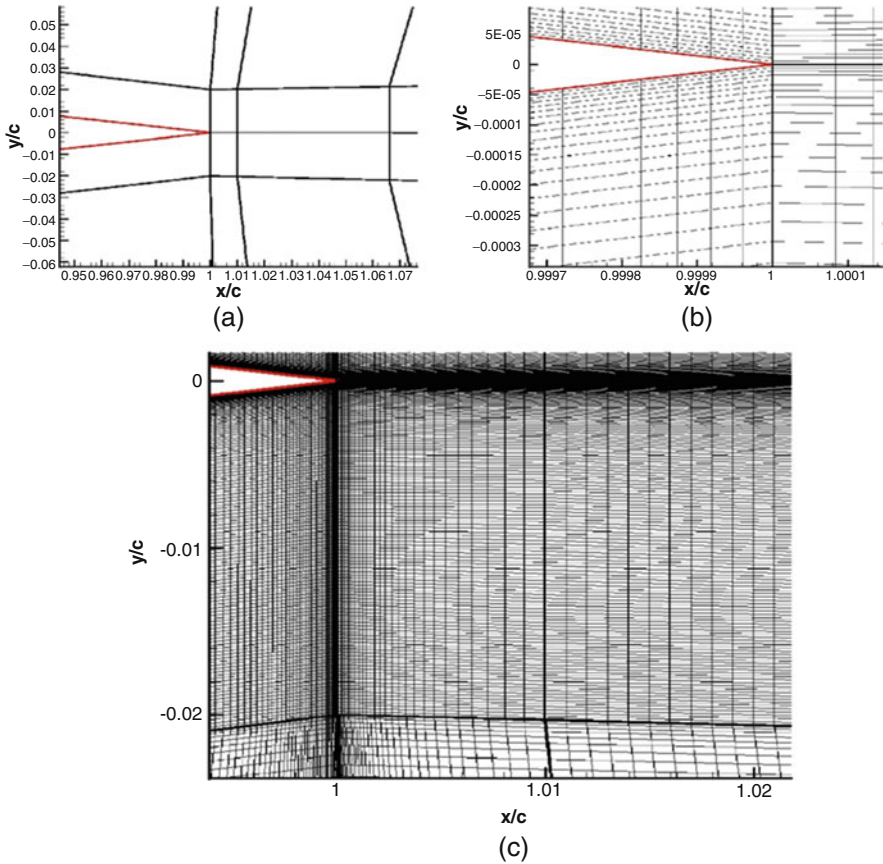
Fig. 2.11 Blocking and mesh spacing for a Gurney at the trailing edge. (**a**) Mesh blocks at trailing edge. (**b**) Detailed mesh close to trailing edge. (**c**) Mesh near trailing edge

the Gurney and the vortical flow structures downstream. The normal spacing to the surface of the aerofoil is 0.5×10^{-6} c which is about an order of magnitude less than that the normal spacing to the Gurney flap. As can be seen in Fig. 2.11c, the block near the trailing edges extends in the normal direction by 2 % of the chord and has been expanded in such a way so that the cells are nearly equally spaced.

This is unlike a normal aerofoil grid where the cells would keep expanding; consequently, these blocks have a large number of cells. This will give a good approximation of any Gurney flap up to a height of 2 % c. The block after the trailing edge between $x/c = (1.01, 1.07)$ has a constant spacing in the x-direction again to help capture the vortical flow in the wake. Figure 2.12 shows the pressure and streamlines for four different Gurney flap sizes at conditions $M = 0.2$, Re = 2.1×10^6, $\alpha = 0$ deg. As the Gurney increases in size, the pressure difference between the two sides of the Gurney also increases, and the flow acceleration near
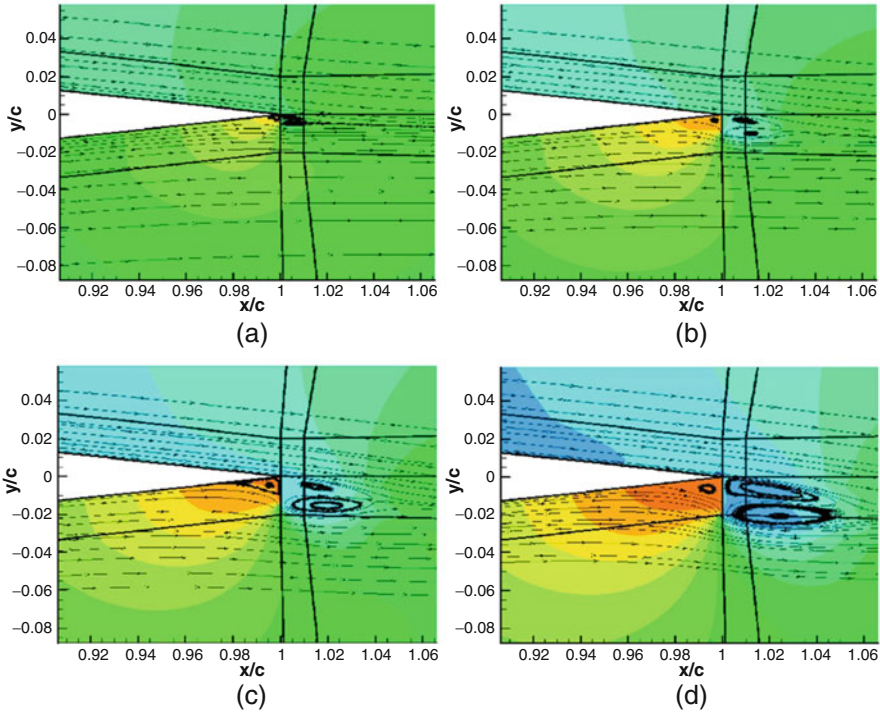
Fig. 2.12 Pressure contours and streamlines for four different heights of Gurneys. NACA 0012, $M = 0.2$, $Re = 2.1 \times 10^6$, $\alpha = 0$ deg, $k - \omega$ SST (Menter 1994). (**a**) $h = 0.5\%$. (**b**) $h = 1.0\%$. (**c**) $h = 1.5\%$. (**d**) $h = 2.0\%$

the trailing edge increases reducing the pressure behind the Gurney. The pressure in front of the Gurney increases due to the larger pocket of stagnant flow.

2.1.3.2   Resolving Flow Details Near the Gurney Flap

Several of the works published in the literature tend to model Gurney flaps using simple flow blockage that did not result in fully resolved flows. In this section, the results obtained with HMB2 for an aerofoil section near a fixed Gurney are put forward as an example of the resolution that should be sought for the Gurney flap computations. This requires fine grids but shows clearly the capability of HMB2 in resolving the details of the flow, and the results presented here should be considered as a benchmark to gauge the correct mesh resolution. In the present study, a C-type mesh of 195,000 nodes is used, 221 nodes were used in the normal direction to the surface with the spacing close to the wall being 0.00001 c, and 189 in the wake with 80 % of them used up to 50 % c distance from the trailing edge. This was necessary to capture the vortices created behind the Gurney flap. Figure 2.13 shows
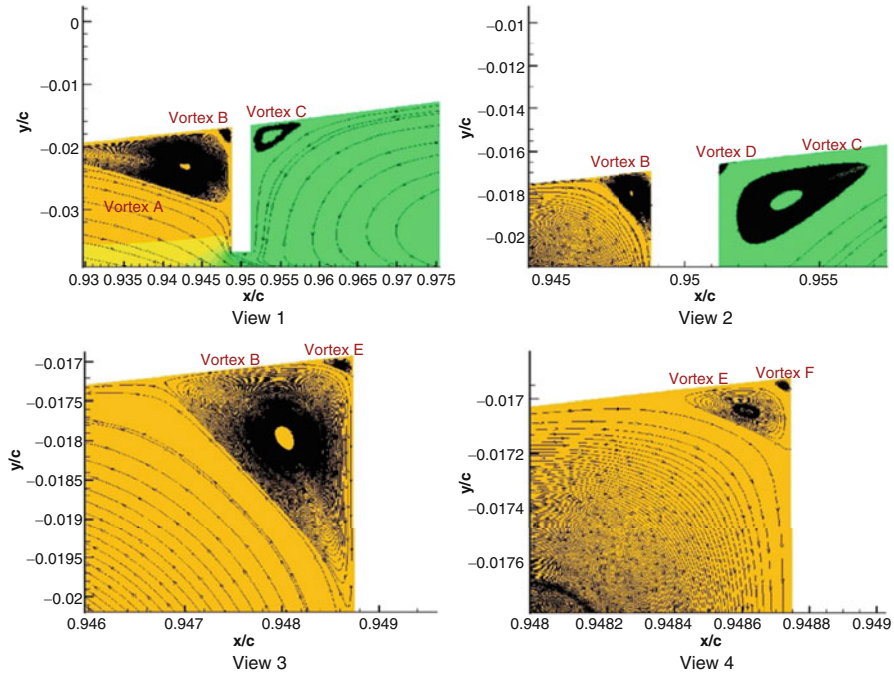
Fig. 2.13 Successive views of the flow near the aerofoil Gurney junction. Streamlines and contours of pressure coefficient are shown

several views of the flow near the corner of the Gurney flap. Pressure contours and streamlines are combined to show the successive resolution of the corner vortices expected in the aerofoil Gurney junction.

The mesh resolution is equally important behind the Gurney flap and near the trailing edge of the section especially since a blunt trailing edge is modelled. This can be seen in Fig. 2.14 where both pressure and turbulent Reynolds number fields are shown again for an NACA 0012 aerofoil with a 2 % c flap near the trailing edge. A further comparison is shown in Fig. 2.15 where results from computations for an infinitely thin Gurney are compared against results at the same conditions but for a Gurney with finite thickness. Such comparisons suggest that for most cases, the infinitely thin Gurney gives a well-resolved representation of the flow and allows easier implementation in HMB2.

Results are obtained for 2 % c Gurney flap located at 95 % c of a NACA 0012 aerofoil. For this case, some experimental data are available and the comparisons are presented in Fig. 2.16. For the clean aerofoil, the CFD results agree well with the experiments. As the size of the Gurney flap increases, there is a small overestimation of the lift and underestimation of the moment, while this difference grows as the aerofoil pitches up. The results for Gurney size 2 % c show that the pressure distribution at the suction side of the aerofoil at zero degrees of incidence
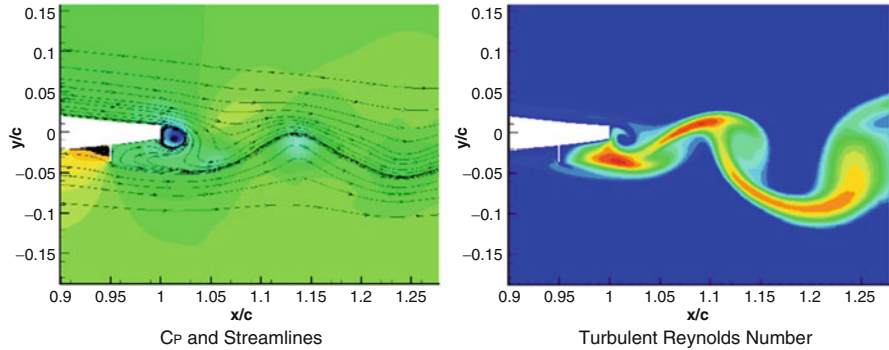
Fig. 2.14 Flow visualisation behind and aerofoil, computed unsteady with a fixed, resolved Gurney and wake. $M = 0.2$, $Re = 2.1 \times 10^6$, $\alpha = 0$ deg, $k - \omega$ SST (Menter 1994)
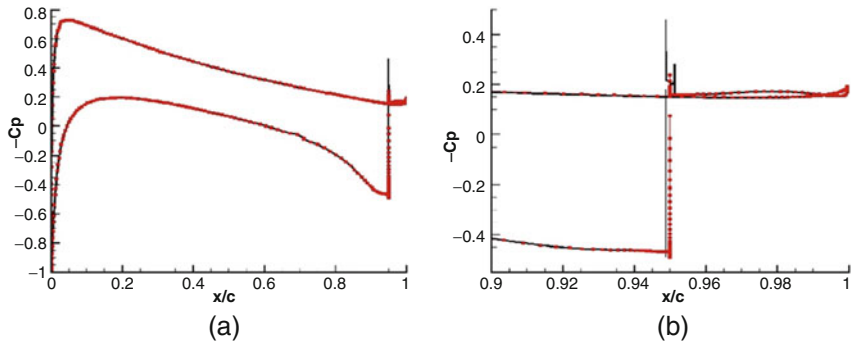

Fig. 2.15 Comparison between thick and thin Gurneys for a NACA 0012 aerofoil with a Gurney of 2 % c length computed at Mach of 0.2 and zero incidence angle. Viscous computations were necessary for this case. *Dotted line* represents the case with the infinitely thin Gurney flap. (**a**) Surface pressure coefficient distribution. (**b**) Zoomed view of the surface pressure coefficient distribution near the trailing edge and Gurney

is under-predicted (Fig. 2.17), which leads to discrepancies in the lift coefficient (Fig. 2.16).

2.1.3.3 Comparison Against Thick Gurney Flap

Next, a NACA23012M aerofoil with a cavity at the trailing edge was tested actuating a virtual Gurney flap linearly. The reduced frequency selected for the oscillation of the flap was $k = 0.1$, and the period of the oscillation was 10π travel times. A non-dimensional time step of 0.001 was used. Figure 2.18 presents the way the Gurney is flagged and actuated.
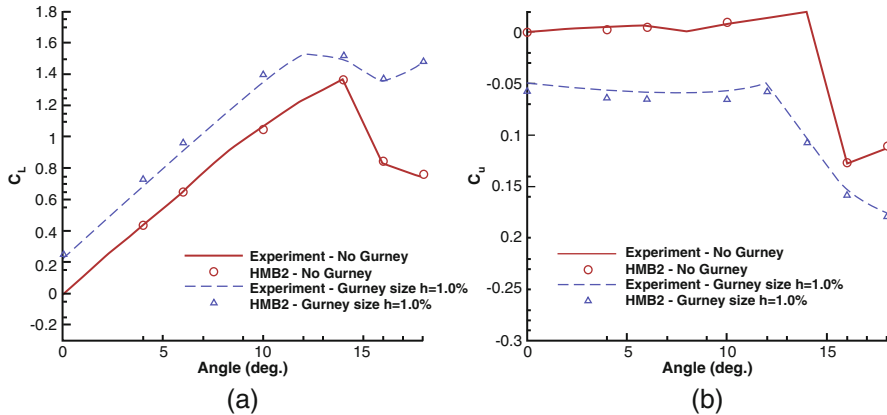
Fig. 2.16 Comparison of loads for different Gurney heights at the trailing edge against experimental data. (**a**) Total lift. (**b**) Total moment

In Fig. 2.18a, the Gurney is fully retracted inside the cavity, while in Fig. 2.18b, it is fully deployed, and it is extended by 1.5 % c outside the cavity. However, the Gurney still exists inside the cavity as the hinge is always attached to the upper wall of the cavity. When the Gurney is retracted, its actual size is 53.9 % of the fully deployed Gurney. Next, the unsteady computation of an actuated Gurney of 1.5 % c at 0.935 c of a NACA23012M aerofoil with a cavity was compared against the same case with a thick Gurney using the Chimera technique. Figure 2.19 presents the unsteady loads for these two cases, while in Figs. 2.20, 2.21 and 2.22, vorticity contours are presented for three different time steps. As can be seen behind the Gurney flap, the vorticity magnitude shows no difference. The only difference is observed inside the cavity where it is assumed to be split into two cavities when the virtual Gurney is used. When the thick Gurney is implemented with the Chimera technique, the flow is allowed to circulate around the Gurney inside the cavity too.

2.2 3D Computations: Gurney Flaps vs Vortex Generators, Comparison Study of Aerodynamic Characteristics

2.2.1 Static Computations

To evaluate the effect of different flow control devices in preventing or delaying the separation of the flow due to stall, several unsteady calculations at fixed pitch as well as pitching-translating wing calculations were conducted as a preliminary stage. During a pitching-translating computation (dMdt), aerofoil or the wing is set to a pitching and translational motion, so that a specific section of a rotor can mimic the conditions of a rotor in forward flight.
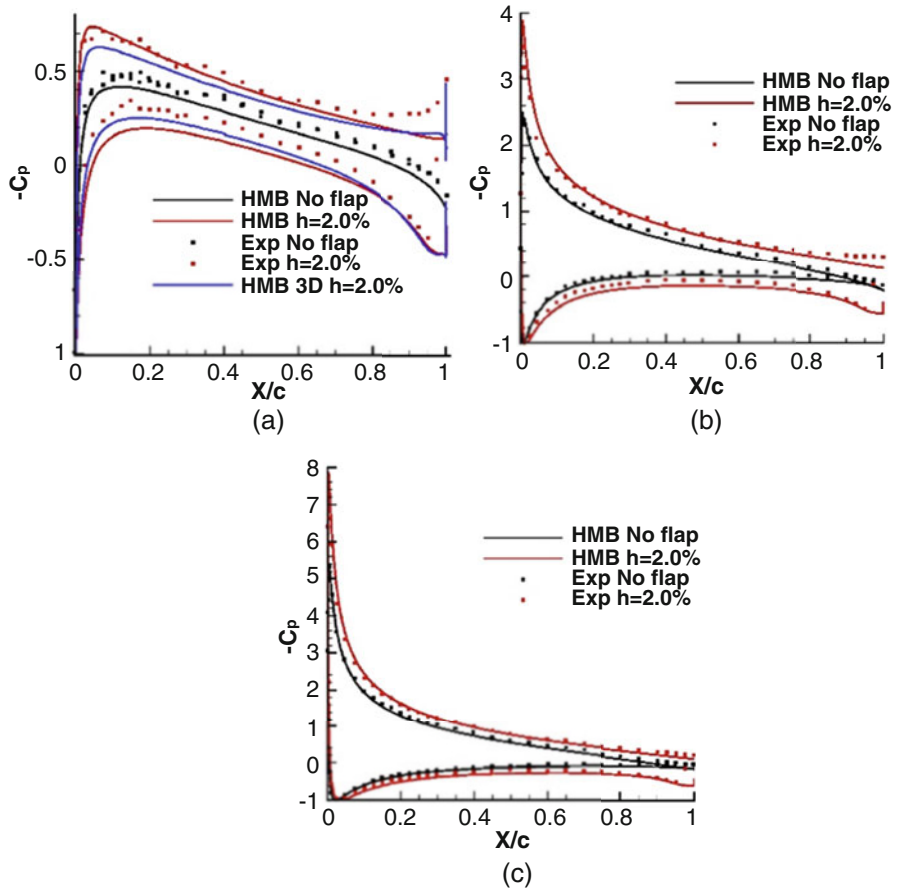
Fig. 2.17 Comparison of pressure distribution of a 2 % Gurney at the trailing edge at different angles of attack. (**a**) Angle of attack 0°. (**b**) Angle of attack 6°. (**c**) Angle of attack 10°

Fixed Gurney flaps and vortex generators (VGs) were studied and compared for the unsteady calculations of a NACA23012M wing of 1.15 c span at fixed pitch. NACA23012M consists the main section used on the rotor case studied in the next chapters. Twenty pairs of counterrotating vortex generator vanes were located at 20 % of the chord from the leading edge. The distance between each pair was 0.05 c, and the angle at which the VGs were set to form a pair was 46°. The size of the grid was approximately four million nodes, while the sliding plane technique was used to keep that size reasonable and the mesh refined close to the VGs area where the formation of the vortices was expected. The VG specifications as well as the mesh topology and the sliding planes used are presented in Figs. 2.23, 2.24 and 2.25. Two sizes of VGs were tested, 0.005 c and 0.01 c. It has to be noted that the sliding planes used for these cases can also be used for a rotor case with vortex generators implemented.

NACA23012M aerofoil with cavity
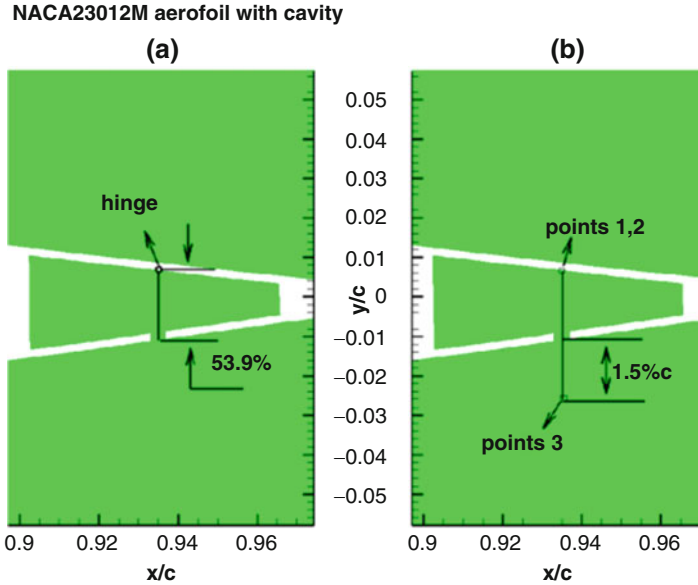
Fig. 2.18 Definition of the actuation of the virtual Gurney used for NACA23012M aerofoil with cavity

Figure 2.26 presents the fixed Gurney flap which is modelled at the trailing edge of the wing and along the whole span. The size of that Gurney is 0.01 c, and the size of the last cell which accommodates the flap is 0.001 c. Different Gurney sizes were tested from 0.001 c to 0.02 c. The Gurney flap was modelled based on the method described in the previous section.

2D symmetry conditions were applied on the boundaries for both cases. The k–ω SST model was used, while the freestream Mach and Reynolds number were 0.2843 and 1.72×10^6, respectively. The results are presented in Figs. 2.27, 2.28 and 2.29. Based on those results, some important remarks can be made. It is obvious that the Gurney flap increases significantly the lift coefficient, but this comes with a drag penalty and increase of the pitching down moments. On the other hand, vortex generators did not affect significantly the aerodynamic loads of the clean wing. However, the effect of VGs becomes stronger at high angles of attack. Moreover, the maximum clean lift coefficient ($L/D = 34.1$) can be achieved by using a Gurney flap at 6.7° less with an increase of the lift to drag ratio at the same time ($L/D = 54.6$), while the use of VGs will result at the same lift coefficient at 1.7° less with similar increase of the L/D ratio ($L/D = 51.5$). By decreasing the size of the Gurney flap at high angles of attack, the effect of the Gurney came closer to one of the vortex generators, while the drag and moment penalties were significantly decreased. This outcome shows that a carefully designed Gurney flap and actuation algorithm can result at the same effect as VGs at high angles of attack, while maintaining its positive effects at low angles of attack.
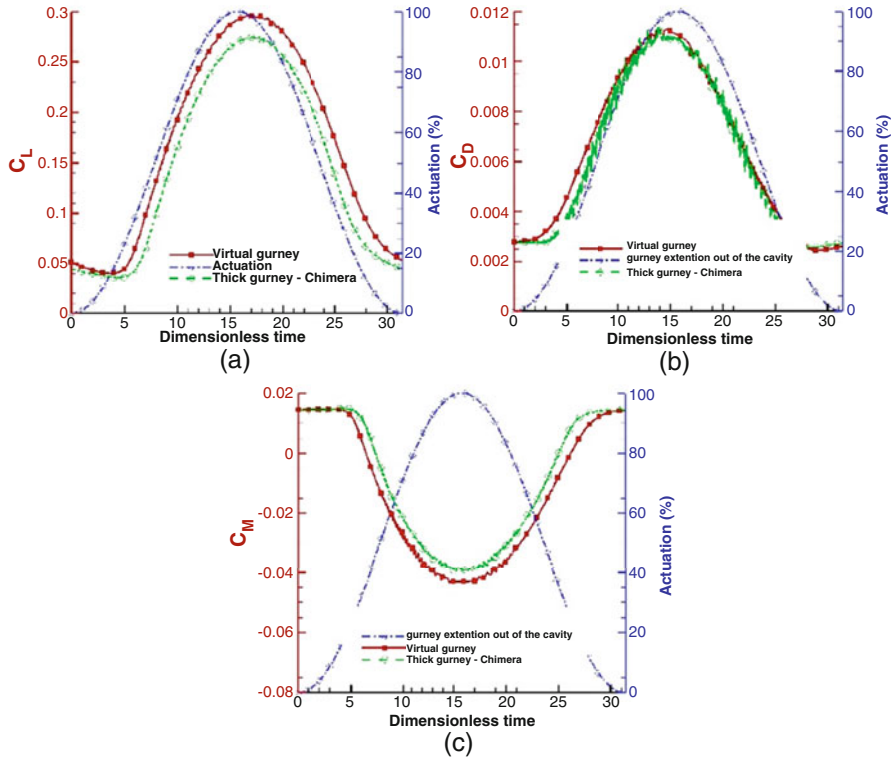
Fig. 2.19 (**a**) Lift, (**b**) drag and (**c**) moment coefficient comparison on NACA23012M aerofoil with cavity and a linearly actuated virtual and thick Gurney flap of 1.5 % c at 93.5 % c, $M = 0.2$, $Re = 0.5 \times 10^6$

2.2.2 Pitching-Translating Wing Computations

To evaluate the effect of the above flow control devices in preventing or delaying the separation of the flow due to retreating blade stall, several dMdt calculations were conducted next. For such computations, the harmonic motion of the wing is given by

$$x = x_0 + \sum_{i=1}^{nhar} x_s \sin{(2kit)} + x_c \cos{(2kit)}$$

where the x_0 is the mean translation, nhar is the number of harmonics, k is the reduced frequency of the first harmonic and x_s and x_c are the coefficients of the sine and cosine contribution of each harmonic. At this study, a NACA23012M wing of 4 chords span was used again with symmetry conditions applied on the boundaries,
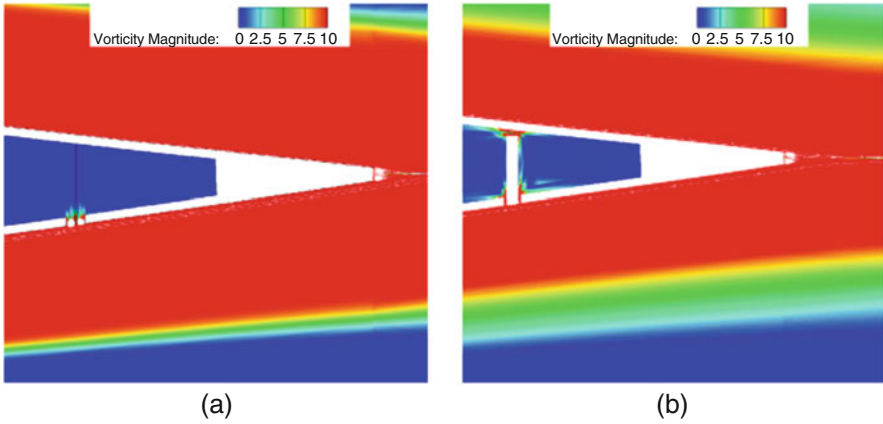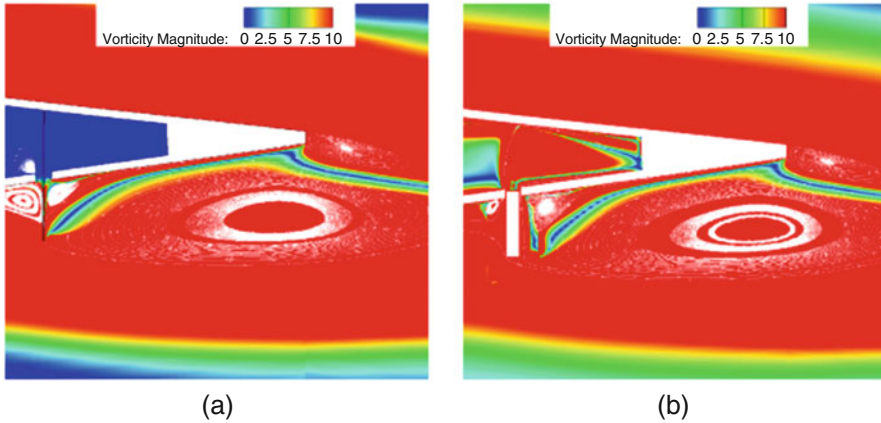
Fig. 2.20 Vorticity magnitude visualisation for a NACA23012M aerofoil with cavity and a linearly actuated virtual (**a**) and thick (**b**) Gurney flap of 1.5 % c at 93.5 % c, $M = 0.2$, Re = 0.5×10^6. The Gurney flap is fully retracted
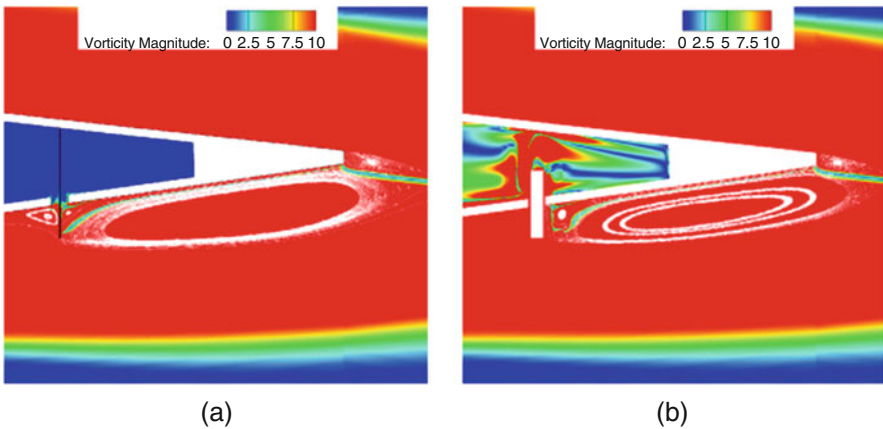
Fig. 2.21 Vorticity magnitude visualisation for a NACA23012M aerofoil with cavity and a linearly actuated virtual (**a**) and thick (**b**) Gurney flap of 1.5 % c at 93.5 % c, $M = 0.2$, Re = 0.5×10^6. The Gurney flap is half actuated

while the pitch and translational schedule were selected based on flight test data of the W3 Sokol helicopter so that the wing experiences retreating blade stall. Both flow control devices covered 30 % of the span of the wing, and the vortex generators of size 0.01 c were fixed, while the Gurney flap of size 0.02 c was actively deployed at the retreating side. On a forward flight case of freestream speed $M_\infty = 0.2052$, a blade section experiences a flow of speed given by

$$M_{\text{section}} = M_{\text{tip}} \frac{r}{R} + M_\infty \sin{(\Psi)}$$

Fig. 2.22 Vorticity magnitude visualisation for a NACA23012M aerofoil with cavity and a linearly actuated virtual (**a**) and thick (**b**) Gurney flap of 1.5 % c at 93.5 % c, $M = 0.2$, Re $= 0.5 \times 10^6$. The Gurney flap is fully actuated

Although the inflow and 3D effects are not taken into account, dMdt is a very good and efficient calculation compared to a rotor case in order to approximate the forward flight effect on a blade section of a rotor.

The wing section simulating the 45 % of the blade radius of W3 Sokol main rotor is pitching down and moving forward (from positive to negative x) with high local speed at the advancing side, while at the retreating side, the local speed is decreased, and the wing is moving backward (from negative to positive x) and it is pitching up. The 20 pairs of counterrotating vortex generators did not alter the *L/D* ratio although they decreased the separated flow due to stall. On the other hand, the active Gurney flap increased the *L/D* ratio by 1.1 %. At the same time, although the separated flow was further decreased compared to the VG case, it is to be noted that the direction of the wake was slightly changed, which, in the case of a rotorcraft, may lead to blade vortex interaction. The pitching down moments that were introduced due to the Gurney can be used to alter the twist distribution on a relative soft blade in torsion which will lead to even lower collective and torque requirement.

Figures 2.30, 2.31 and 2.32 show the detached flow for three different cases used for this study. As can be seen, the active Gurney flap was the device which delayed the onset of the separation more. However, the schedule of the actuation of the Gurney must be carefully designed to lead to aerodynamic performance enhancement.

Fig. 2.23 (**a**) NACA23012M
with 20 pairs of
counterrotating vortex
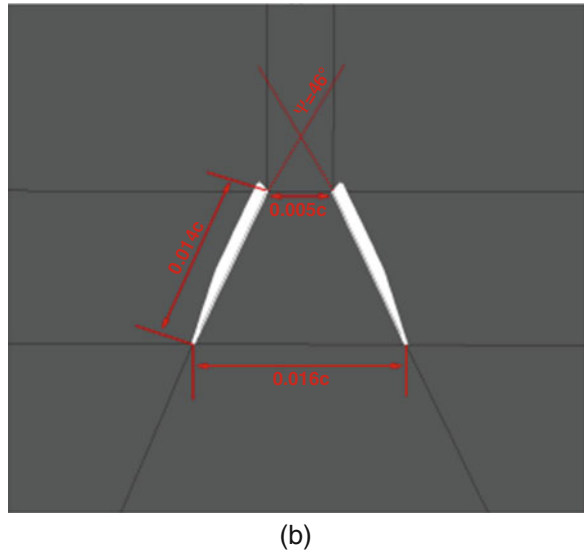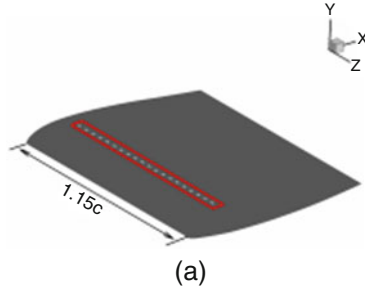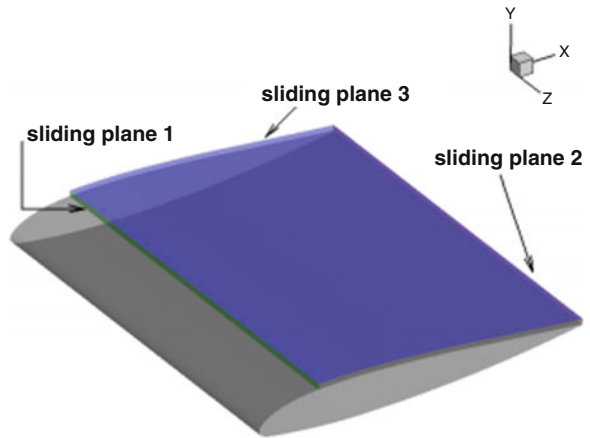generators, (**b**) specification
of vortex generator vane

(a)
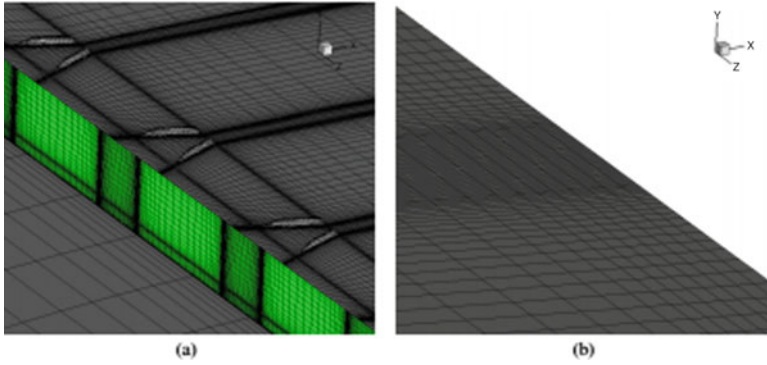

(b)

Fig. 2.24 Overview of
sliding planes used for grid
refinement

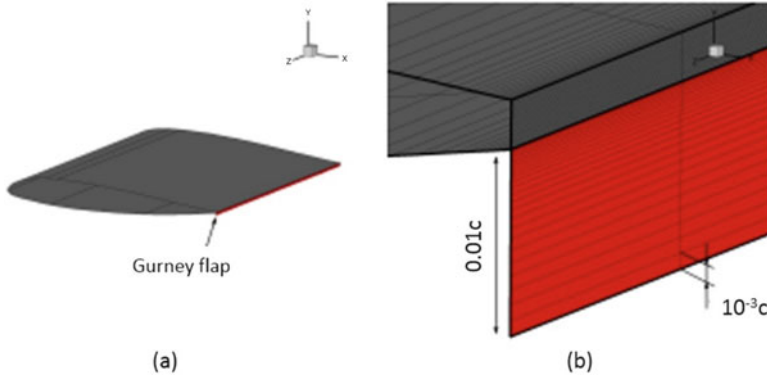**Fig. 2.25** Overview of the mesh (**a**) near the vortex generators and (**b**) near the trailing edge

Fig. 2.26 (**a**) NACA23012M wing with fixed Gurney flap at the trailing edge and (**b**) a close view of the flap and surface mesh near the trailing edge

2.2.3 Observations

The main aerofoil sections used on the W3-Sokol main rotor were initially studied with CFD to investigate the change of the aerodynamic performance resulted by some modifications on the baseline NACA23012. Next, a preliminary study took place, and two flow control devices were tested on the modified NACA23012M section. The main target of the study was to identify the advantages and limitations

Fig. 2.27 (**a**) Lift and (**b**) drag coefficient comparison between Gurney flap and vortex generators for a wing NACA23012M, $M = 0.2843$, $Re = 1.72 \times 10^6$
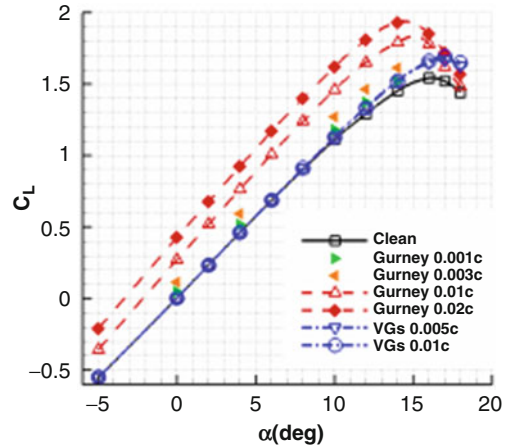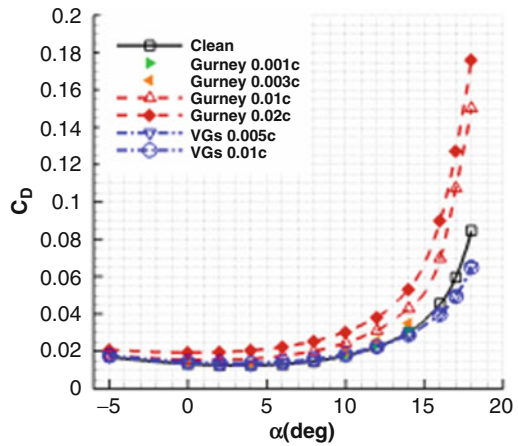
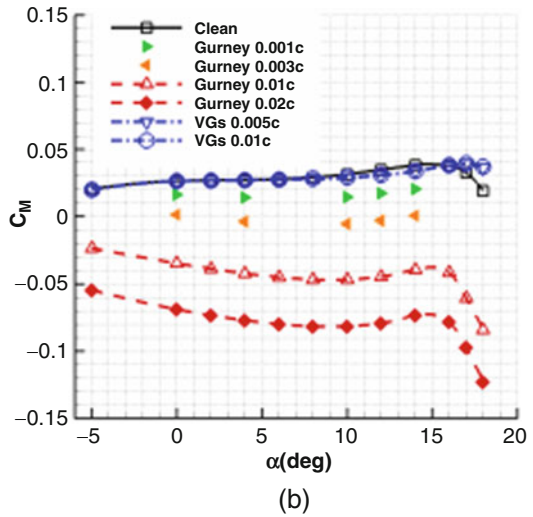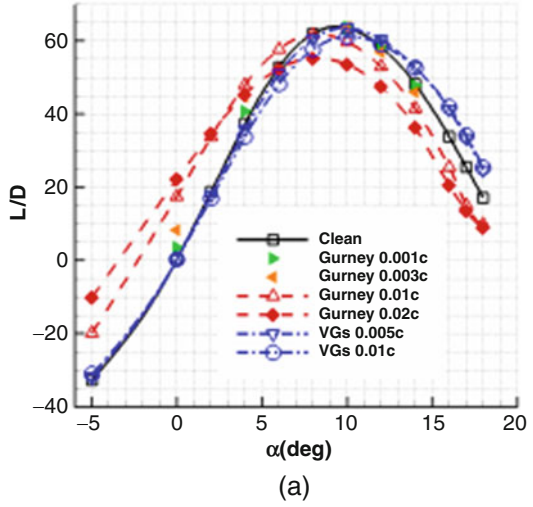of those mechanisms, as well as their potential use for delaying retreating blade stall separation of the flow. The active Gurney flap proved to be more effective, and it can be used to alter the aerodynamic performance of the blade not only by affecting its aerodynamics but also by changing locally the pitch of the blade section.
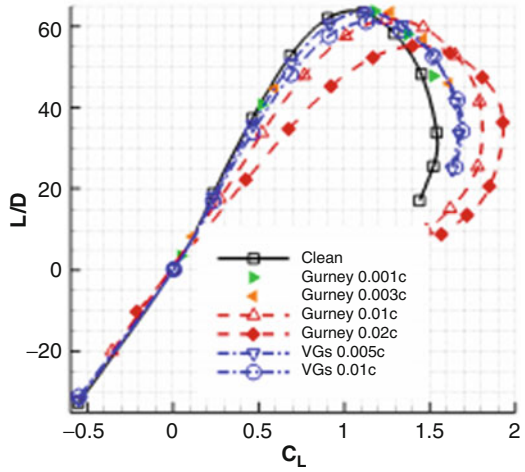
Fig. 2.29 Lift over drag ratio versus lift coefficient comparison between Gurney flap and vortex generators for a wing NACA23012M, $M = 0.2843$, $\mathrm{Re} = 1.72 \times 10^6$
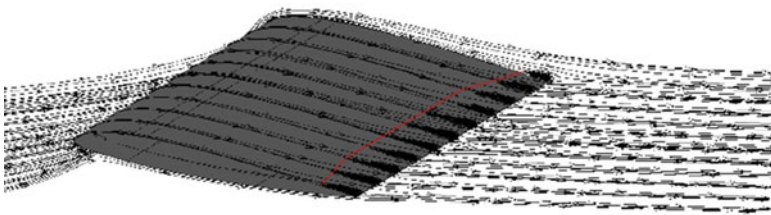

Fig. 2.30 Visualisation of the streamlines along the span of the clean wing. The *red line* indicates the onset of the separation
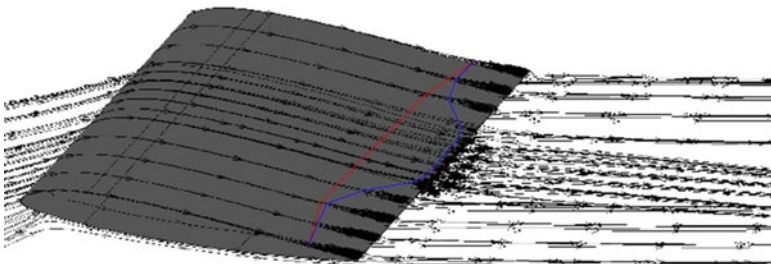

Fig. 2.31 Visualisation of the streamlines along the span of the wing with active Gurney flap. The *red* and *blue line* indicate the onset of the separation of the clean wing and the wing with active Gurney flap, respectively
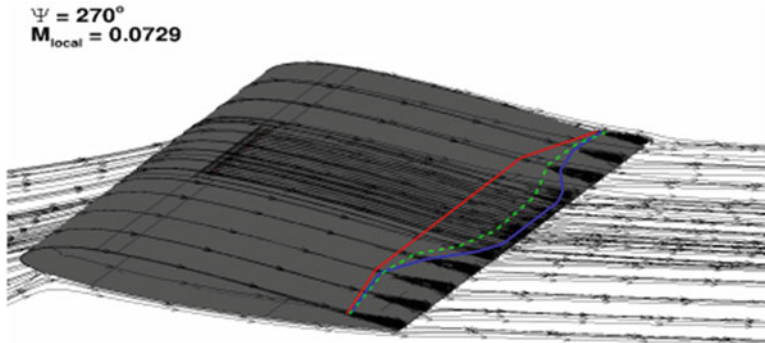
Fig. 2.32 Visualisation of the streamlines along the span of the wing with vortex generators. The *dashed green line* indicates the onset of the separation of the wing with VGs

References

Albada GD, Leer BV, Roberts W (1982) A comparative study of computational methods in cosmic gas dynamics. Astron Astrophys 108:76–84

Jameson A (1991) Time dependent calculations using multigrid, with applications to unsteady flows past airfoils and wings. Technical Report, AIAA-91-1596

Menter FR (1994) Two-equation eddy-viscosity turbulence models for engineering applications. AIAA J 32(8):1598–1605

Min B, Sankar LN, Rajmohan N, Prasad J (2009) Computational investigation of gurney flap eefect on rotors in forward flight. J Aircr 46(6):1957–1964

Osher S, Chakravarthy S (1983) Upwind schemes and boundary conditions with applications to Euler equations in general geometries. Comput Phys 50(3):447–481

Steijl R, Barakos GN (2008a) A computational study of the advancing side lift phase problem. J Aircr 45(1):246–257

Steijl R, Barakos GN (2008b) Sliding mesh algorithm for CFD analysis of helicopter rotor-fuselage aerodynamics. Int J Numer Methods Fluids 58(5):527–549

Steijl R, Barakos GN, Badcock K (2006) A framework for CFD analysis of helicopter rotors in hover and forward flight. Int J Numer Methods Fluids 51(8):819–847

Wang JJ, Li YC, Choi KS (2008) Gurney flap—lift enhancement, mechanisms and applications. Progress Aerosp Sci 44(1):22–47